PNAS RESEARCH ARTICLE | ENGINEERING

Lattice materials with topological states optimized on demand

Pegah Azizi[a,1], Rahul Dev Kundu[b,1], Weichen Li[b], Kai Sun[c], Xiaojia Shelly Zhang[b,2], and Stefano Gonella[a,2]

Affiliations are included on p. 8.

Edited by Wei Chen, Northwestern University, Evanston, IL; received March 24, 2025; accepted July 9, 2025 by Editorial Board Member Yonggang Huang

Topological states of matter, first discovered in quantum systems, have opened new avenues for wave manipulation beyond the quantum realm. In elastic media, realizing these topological effects requires identifying lattices that support the corresponding topological bands. However, among the vast number of theoretically predicted topological states, only a small fraction has been physically realized. To close this gap, we present a strategy capable of systematically and efficiently discovering metamaterials with desired topological state. Our approach builds on topological quantum chemistry, which systematically classifies topological states by analyzing symmetry properties at selected wavevectors. Because this method condenses the topological character into mathematical information at a small set of wavevectors, it encodes a clear and computationally efficient objective for topology optimization algorithms. We demonstrate that, for certain lattice symmetries, this classification can be further reduced to intuitive morphological features of the phonon band structure. By incorporating these band morphology constraints into topology optimization algorithms and further fabricating obtained designs, we enable the automated discovery and physical realization of metamaterials with targeted topological properties. This methodology establishes a paradigm for engineering topological elastic lattices on demand, addressing the bottleneck in material realization and paving the way for a comprehensive database of topological metamaterial configurations.

topology optimization | topological mechanical | mechanical metamaterials | vibrometry testing | wave control

Significance

The legacy of decades of phononics research is a sharp awareness of the wave manipulation capabilities of elastic metamaterials. Incorporating optimization methods is also bringing metamaterials technology closer to widespread adoption in engineering design. The most recent leap broadening the horizon of metamaterials functionalities is traceable to the injection of notions of topological states of matter. However, these physics have yet to be systematically incorporated into design frameworks, due to lacking efforts to effectively encode principles of topology into drivers of optimization. Offering a much-needed synthesis between these perspectives, we provide criteria to distill salient topological attributes and recast them as objectives of optimization algorithms, enabling computerized design and physical realization of libraries of metamaterials with on-demand topological states.

The ability to control mechanical waves and vibrations is a highly sought-after attribute in material systems across engineering and materials science applications. Homogeneous solid media lack the architectural complexity required to manipulate the propagation of elastic waves beyond conventional regimes. This limitation has sparked growing interest in architected materials and metamaterials. Metamaterials owe their properties not to their composition but to the geometry of their internal architecture which, in the case of lattice materials, is spatially periodic. Through careful design, elastic metamaterials provide unprecedented control of wave propagation, enabling notable phenomena such as bandgap (BG) opening and tuning, directivity, negative refraction, and super-focusing (1–9).

An additional dimension to this array of capabilities has emerged from the injection of notions of topology. Through a topological classification of wave descriptors defined in the frequency-wavevector space (*k-space topology*), and by adapting to elastodynamics selected concepts of topological phases of matter originally introduced to describe quantum and electronic phenomena, we can elicit and interpret effects that elude conventional phononics analysis. This philosophy has opened the field of topological mechanical metamaterials, material systems that exhibit static and dynamic regimes that are robust against defects and perturbations, e.g., polarized elasticity and one-way edge and interface states (10–19). These topologically protected phenomena are associated with the presence of topological bands in the phonon spectrum. Consequently, the ability to recognize the existence of such bands—and, more importantly, to promote their emergence when designing new materials—has become a crucial objective.

The recently developed framework of Topological Quantum Chemistry (TQC) offers a streamlined approach to classifying and identifying topological bands based on symmetry arguments (20–28). By relying exclusively on the inspection and classification of irreducible representation labels (the so-called *irreps*) evaluated at the high-symmetry points (HSPs) of the Brillouin zone (BZ), TQC simplifies the identification of symmetry-protected topological states (TSs), offering an efficient and practical alternative to computationally intensive methods that traditionally require detailed knowledge of Bloch wave functions across the entire BZ to define topological invariants. In essence, the

The authors declare no competing interest.

This article is a PNAS Direct Submission. W.C. is a guest editor invited by the Editorial Board.

[1]P.A. and R.D.K. contributed equally to this work.

[2]To whom correspondence may be addressed. Email: zhangxs@illinois.edu or sgonella@umn.edu.

This article contains supporting information online at https://www.pnas.org/lookup/suppl/doi:10.1073/pnas.2506787122/-/DCSupplemental.

Published August 5, 2025.

irreps capture how the eigenfunctions—in elastodynamics, the unit cell mode shapes—transform under various symmetry operators. Formally, a band structure is deemed topologically nontrivial if its irreps cannot be matched to those of any atomic insulator, indicating a state that, by definition, cannot be described by symmetric localized Wannier functions (20). The Bilbao Crystallographic Server (BCS) compiles all possible atomic insulators by combining lattice and orbital types in terms of irreps, thus providing a comprehensive reference to determine whether a given band structure is topologically trivial or hosts symmetry-protected TSs (29–32). Recently, researchers have invoked the TQC framework to identify topological bands (33) in photonic crystals (34), acoustic (35), and phononic metamaterials (36–39).

A promising approach for discovering mechanical metamaterials with prescribed properties is inverse design through topology optimization (TO), a design methodology based on strategic spatial allocation of material phases in a given design domain guided by mechanics-based algorithms (40–42). Providing broader design freedom than intuition- or trial-and-error-based methods, TO has been applied to the inverse design of phononic structures with the goal of optimizing certain wave control capabilities, such as BG widening or lowering (43–51), negative refraction (52), acoustic and photonic cavities (53, 54), and elastic wave barrier and absorber (55, 56). More recently, TO has been employed to design topological insulators by enforcing global signatures of topological behavior (e.g., the emergence of interface states) as optimization objectives (57), by promoting Dirac cones to obtain quantum spin Hall analogs (58–61) or quantum valley Hall analogs (62, 63), or by directly optimizing topological invariants (64). Despite these advances, the direct encoding of phonon band topology criteria into TO frameworks remains largely unexplored due to the inherent challenges of mathematically capturing the unique conditions that underlie topological phenomena and translating them into efficient drivers for the optimization algorithms. In addition, theoretical studies have vastly outpaced experimental realizations of TSs, with only a relatively small subset being directly confirmed experimentally.

This gap underscores the need for a versatile inverse design framework that systematically encodes the topological descriptors directly into the optimization process, thus enabling the discovery of metamaterials that display desired topological properties while retaining the structural characteristics that make them amenable to physical fabrication and testing. In parallel to the primary objective of guaranteeing the emergence of desired topological bands on demand, such optimization framework could ideally be set up to simultaneously pursue other (secondary) desired targets, such as tuning BG onsets and widths to target desired operational frequency regimes. This set of goals involves the nontrivial task of distilling the topological requirements of bands into a parsimonious set of rigorous band descriptors that can be expressed mathematically and effectively incorporated into optimization algorithms. The TQC approach discussed above, which simplifies the topology of bands to mere symmetry considerations, constitutes an ideal tool around which we can construct our design strategy. We emphasize that, in this work, the term topology appears in two distinct contexts: 1) when defining topological bands, we refer to the so-called k-space topology of the momentum space; 2) when we discuss cell configurations, we refer to the real-space topology of their geometric layout; accordingly, when we talk about topology optimization, we refer to a computational design technique that spatially distributes material within a domain to target specific physical properties.

In the remainder of this paper, we will propose a strategy to address these design and physical demonstration needs, leveraging the integration of two powerful and complementary tools: 1) a method for topological classification of bands, based on TQC and boosted by recent discoveries that link TQC criteria to band morphology requirements; 2) a TO strategy specifically tailored to promote the emergence of topological features through the incorporation of key band morphology descriptors as drivers of the optimization algorithms. The discovered metamaterial is then physically fabricated and experimentally demonstrated to possess the target topological properties. The conceptual steps of this strategy are summarized by pictorial highlights in Fig. 1. (*A*) We start from a general classification philosophy of band topology, rooted in principles of group and graph theory and formalized by TQC. Here, we invoke a key finding from our recent study, which pinpoints the emergence of band topology to few band morphological attributes that can be assessed through agile band inspection. (*B*) We encode these morphological requirements mathematically as objectives and constraints of TO algorithms to enable the automatic discovery of metamaterials. (*C*) We comprehensively explore the nonconvex design space of lattices to compile libraries of configurations with a common desired topological character as primary attribute and a plethora of secondary phononic features. (*D*) Finally, we test the dynamics of selected configurations using physical prototypes to confirm the emergence of the desired band topology through an a-posteriori assessment of the morphology of experimentally reconstructed bands. In the next section, we will discuss all these steps in detail.

Results and Discussion

Fundamental Relations Between TQC and Band Morphology. In this section, we outline the key conceptual steps of our proposed framework for designing lattice materials with desired TSs based on band morphology criteria. Our starting point leverages a key intuition gained in our previous study on the dynamics of structural kagome metamaterials (37). This study adopted the symmetry arguments of TQC to assess the topological character of bands, thus extending to elastic lattice materials a framework originally proposed for -and tested against- quantum and electronic systems. Recall that a key insight from TQC is the notion that the topological character of bands can be assessed by looking at certain symmetry indicators, known as "irreps," which capture how the eigenfunctions transform under a number of symmetry operators. The landscapes of irreps for a band, or cluster of isolated bands, that are associated with trivial bands are cataloged in the BCS; hence, a band of a lattice belonging to a given symmetry class is deemed topological if it does not conform to any of the tabulated landscapes of irreps for that symmetry class.

Furthermore, in ref. 37 a connection was demonstrated between the topological character of the bands and certain morphological attributes of the corresponding branches in the band diagram. It was shown that, for the considered symmetry class ($p31m$ wallpaper group), the existence of two isolated bands that cross exclusively at the HSP Γ, without retouching at any other HSPs, i.e., K and M, constitutes a necessary and sufficient condition to guarantee the topological character of those bands. In essence, the matter of topological classification reduces to an agile and intuitive inspection of a parsimonious set of morphological branch descriptors, which serve as proxies for the TQC irreps. This powerful observation implies that one can ascertain the emergence of topology from experimental or numerical data by simply reconstructing the bands from the

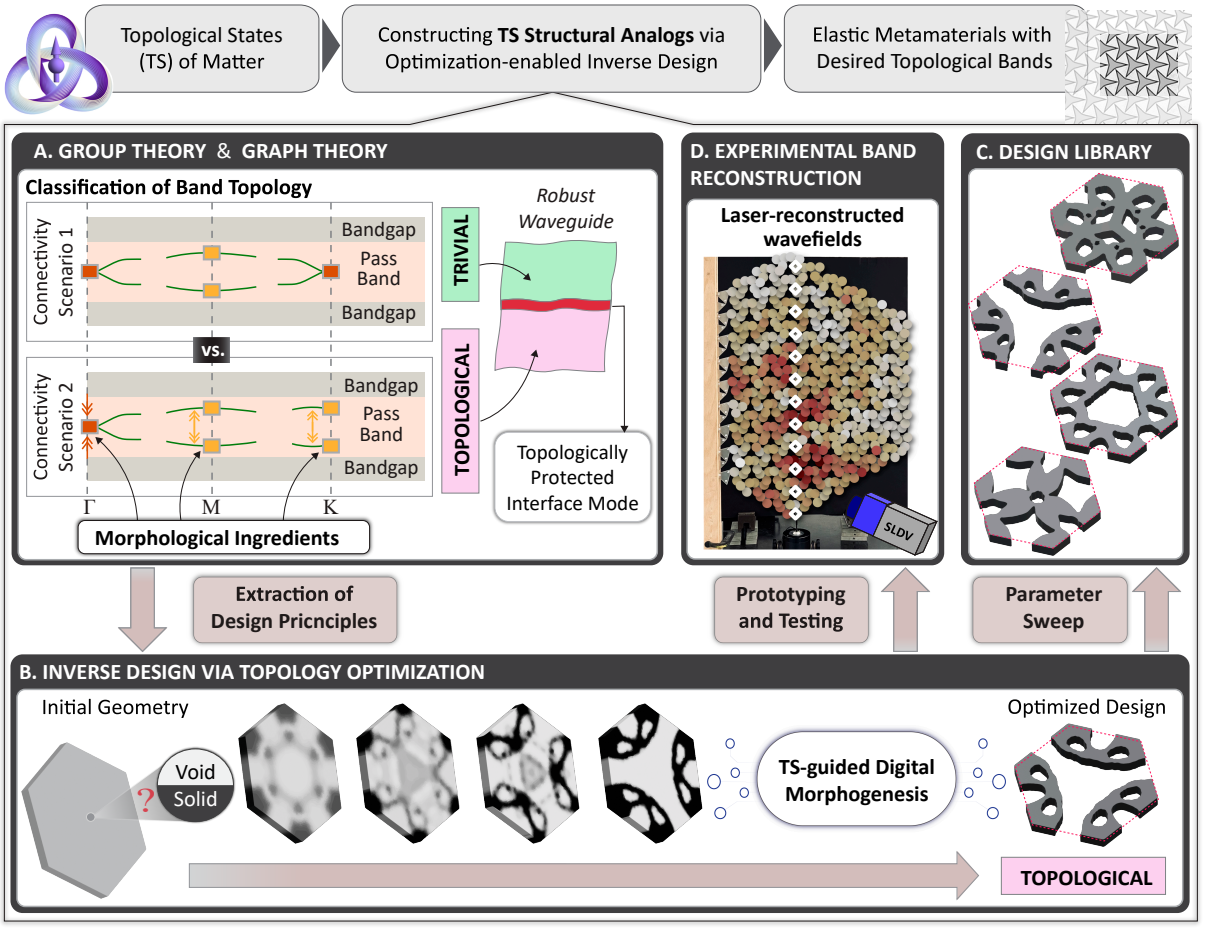

Fig. 1. Conceptual schematic of the proposed framework. (*A*) Two connectivity scenarios within the *p*31*m* symmetry group, corresponding to trivial and topological bands as identified by topological quantum chemistry (TQC)-enabled band classification, along with a potential application. Morphological band features identified as key drivers for the topology optimization (TO) algorithm. (*B*) Digital morphogenesis inverse design process via the proposed TO framework, enabling automatic discovery of metamaterials with desired topological features, showing intermediate steps and an optimized configuration. (*C*) A selection of generated configurations, demonstrating the diverse patterning achieved. (*D*) Laser vibrometry testing of a fabricated prototype, used to experimentally reconstruct and validate the band diagram.

measured response and assessing their morphology—a routine operation in phononics that can be carried out agnostically, even in the absence of a precise model of the lattice cell.

The ability to classify the mechanical performance in terms of a discrete set of parameters provides a golden platform for the development of optimization frameworks for structural and material design. Not only can the morphology criteria be used directly to characterize the topological character of the bands; they can also serve as drivers of an automated inverse design process aimed at discovering new lattice configurations of arbitrary complexity with desired topological attributes. The idea is to construct an optimization algorithm in which such criteria are embedded either as objective functions or constraints of the optimization problem. In the next section, we elucidate this idea targeting, as a benchmark example, the band morphology observed for finite-frequency topological bands in lattices of the *p*31*m* wallpaper group.

A Band Morphology-Driven TO Strategy to Find TSs. The first step toward automated discovery of lattice configurations via band morphology-driven TO is to identify the primary design principles, i.e., the desired topological attributes of the targeted phononic behavior. Since we target finite-frequency regimes, and we expect two acoustic modes in the phonon spectrum, we naturally focus on bands 3 and 4 as the lowest pair of modes that can be spectrally isolated. In the case of the *p*31*m* wallpaper group lattice class, following ref. 37, the primary design principles to enforce topological attributes for those bands boil down to the realization of the following set of band characteristics:

1) enforce a band crossing at the HSP Γ, while maintaining gaps at the HSPs M and K between bands 3 and 4;
2) ensure the complete isolation of band 3 (4) from band 2 (5);

The next step is to translate these requirements into mathematical expressions, i.e., differentiable functions that can be encoded in gradient-based optimization algorithms. The optimization tasks can be classified into two major categories—1) merging or opening gaps between specific bands at HSPs only, and 2) complete isolation of different bands. For the first category, we simply express the gaps between bands m and n at the HSP $t \in \{\Gamma, \mathrm{K}, \mathrm{M}\}$ as

$$\Delta\lambda_t^{(m,n)} = \lambda_t^{(m)} - \lambda_t^{(n)}, \quad (m \geq n), \qquad [1]$$

where λ_t represents the squared eigenfrequency ω_t obtained by solving the generalized eigenvalue problem $\left(\hat{\mathbf{K}}_t - \omega_t^2 \hat{\mathbf{M}}_t\right)\boldsymbol{\phi}_t = \mathbf{0}$. Here, $\hat{\mathbf{K}}_t$ and $\hat{\mathbf{M}}_t$ are the reduced stiffness and mass matrices

considering Bloch periodic boundary conditions evaluated at point t, and we assume the eigenvector $\boldsymbol{\phi}$ is normalized w.r.t. $\hat{\mathbf{M}}$, i.e., $\boldsymbol{\phi}\cdot\hat{\mathbf{M}}\boldsymbol{\phi}=1$. Here, opening (or closing) the gap $\Delta\lambda_t^{(m,n)}$ corresponds to opening (or closing) the gap $\Delta\omega_t^{(m,n)}$ in the band diagram, and therefore we equivalently use $\Delta\lambda_t^{(m,n)}$ in the optimization formulations for simplicity.

The second category, i.e., the complete isolation of band m from band n can also be achieved by evaluating the same expression $\Delta\lambda_j^{(m,n)}$ of Eq. **1** at all wavevector points j and enforcing them to be nonzero. Ideally, all points along the BZ should be sampled to ensure complete band isolation, but this is computationally prohibitive as each sampled point requires solving an eigenvalue problem. To address this, we enforce a total BG, which is a stricter condition for band isolation, while sampling only at the three HSPs Γ, M, and K for j in the optimization. The BG between bands m and n, sampled at the HSPs, can be expressed as

$$\tilde{\Delta}\lambda^{(m,n)}=\frac{1}{\tau_{\mathrm{KS}}[1/\lambda_j^{(m)}]}-\tau_{\mathrm{KS}}[\lambda_j^{(n)}],\quad (m\geq n), \qquad [2]$$

where τ_{KS} is the KS-aggregation function (65) given as

$$\tau_{\mathrm{KS}}[(\cdot)_j]=(\cdot)_{\max}+\frac{1}{\beta}\log\left(\sum_j e^{\beta((\cdot)_j-(\cdot)_{\max})}\right),\quad \text{with, } (\cdot)_{\max}=\max_{j=\Gamma,\mathrm{K},\mathrm{M}}\{(\cdot)_j\} \qquad [3]$$

which provides a smooth approximation of the maximum operator using a smoothness parameter $\beta\in[1,\infty)$. To verify complete spectral isolation, we evaluate the band morphology across all points in the BZ after optimization.

Using Eqs. **1** and **2**, we now construct an optimization problem where the merging of bands 3 and 4 at Γ point is promoted through the objective function and all other criteria are realized through different constraint functions. A volume constraint is included in the formulation, although it is not essential to achieve our target topological band characteristics. The optimization problem is formulated as

$$\begin{aligned}
&\min_{\boldsymbol{z}}\ J(\bar{\boldsymbol{z}})=\Delta\lambda_\Gamma^{(4,3)}(\bar{\boldsymbol{z}})\\
&\text{s.t. } g_1(\bar{\boldsymbol{z}})=-\Delta\lambda_\mathrm{M}^{(4,3)}(\bar{\boldsymbol{z}})+\varepsilon_\mathrm{M}\leq 0,\\
&\quad g_2(\bar{\boldsymbol{z}})=-\Delta\lambda_\mathrm{K}^{(4,3)}(\bar{\boldsymbol{z}})+\varepsilon_\mathrm{K}\leq 0,\\
&\quad g_3(\bar{\boldsymbol{z}})=-\tilde{\Delta}\lambda^{(3,2)}(\bar{\boldsymbol{z}})+\varepsilon_{\mathrm{BG1}}\leq 0,\\
&\quad g_4(\bar{\boldsymbol{z}})=-\tilde{\Delta}\lambda^{(5,4)}(\bar{\boldsymbol{z}})+\varepsilon_{\mathrm{BG2}}\leq 0,\\
&\quad g_5(\bar{\boldsymbol{z}})=V(\bar{\boldsymbol{z}})-V^*\leq 0,\\
&\quad z_e\in[0,1],\qquad e=1,\ldots,N_e,\\
&\text{with } \left(\hat{\mathbf{K}}_j(\bar{\boldsymbol{z}})-\lambda_j\hat{\mathbf{M}}_j(\bar{\boldsymbol{z}})\right)\boldsymbol{\phi}_j=\mathbf{0},\ j=\{\Gamma,\mathrm{M},\mathrm{K}\},
\end{aligned} \qquad [4]$$

where $\boldsymbol{z}$ is the design variable, $\bar{\boldsymbol{z}}$ is the physical variable, V^* is the maximum allowable volume fraction, and ε_M, ε_K, $\varepsilon_{\mathrm{BG1}}$ and $\varepsilon_{\mathrm{BG2}}$ are the prescribed constraint tolerances representing lower bounds of desired HSP gaps or BGs. The physical variable $\bar{\boldsymbol{z}}$ is obtained through filtering (66–69) and Heaviside projection (70) on the design variable $\boldsymbol{z}$, and it represents solid or void regions in the design domain with values 1 and 0, respectively. This inverse design process that embeds the insights from TQC into a TO framework for automated discovery of topological lattices is summarized in Fig. 2. Specifically, Fig. 2*A* illustrates the periodic design domain that conforms to the crystallographic symmetry and periodicity requirements for the chosen $p31m$ group, Fig. 2*B* presents the primary design principles for the band morphology and corresponding mathematical expressions in the form of an optimization problem using a simplified representation of Eq. **4**, and Fig. 2*C* shows the resulting optimized design satisfying all design principles in Fig. 2*B*, as verified in the next subsection with rigorous numerical and experimental investigations. We note that a unique advantage of using optimization-driven morphogenesis is that, by varying the forms of the objective and constraint functions in Eq. **4**, we can attain a diverse collection of optimized mechanical lattices with dissimilar geometries yet identical topological characteristics that meet the same primary principles. The database of these lattices are presented and discussed in a later section and in *SI Appendix*.

Numerical and Experimental Extraction of Topological Signatures. We now proceed to interrogate the outcome of the TO algorithm by performing a full phononic analysis of the configuration that has emerged from the optimization and, specifically, assessing the establishment of topological character. The generated configuration is shown in the *Inset* of Fig. 3*A* along with its lattice vectors $\mathbf{e}_1$ and $\mathbf{e}_2$. The unit cell is discretized into a mesh of 4-node isoparametric 2D plane-stress elements and subjected to a canonical FE-based Bloch analysis (*Materials and Methods*). The resulting band diagram, limited to the six lowest bands, is shown in Fig. 3*A*. A visual inspection of the band diagram immediately reveals that the morphological requirements are indeed satisfied: 1) bands 3 to 4 are isolated, 2) they cross at the HSP Γ, and 3) a gap exists at the HSPs M

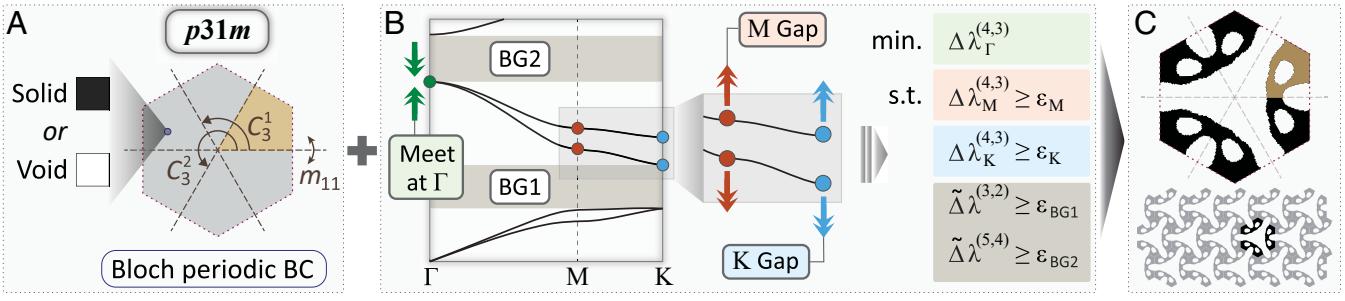

Fig. 2. Digital morphogenesis inverse design via band morphology-driven topology optimization. (*A*) Design domain, boundary conditions (BC), and candidate material phases. (*B*) Target band morphology translated and encoded into an optimization formulation. (*C*) Discovered metamaterial design with desired topological features and its tessellated assembly.

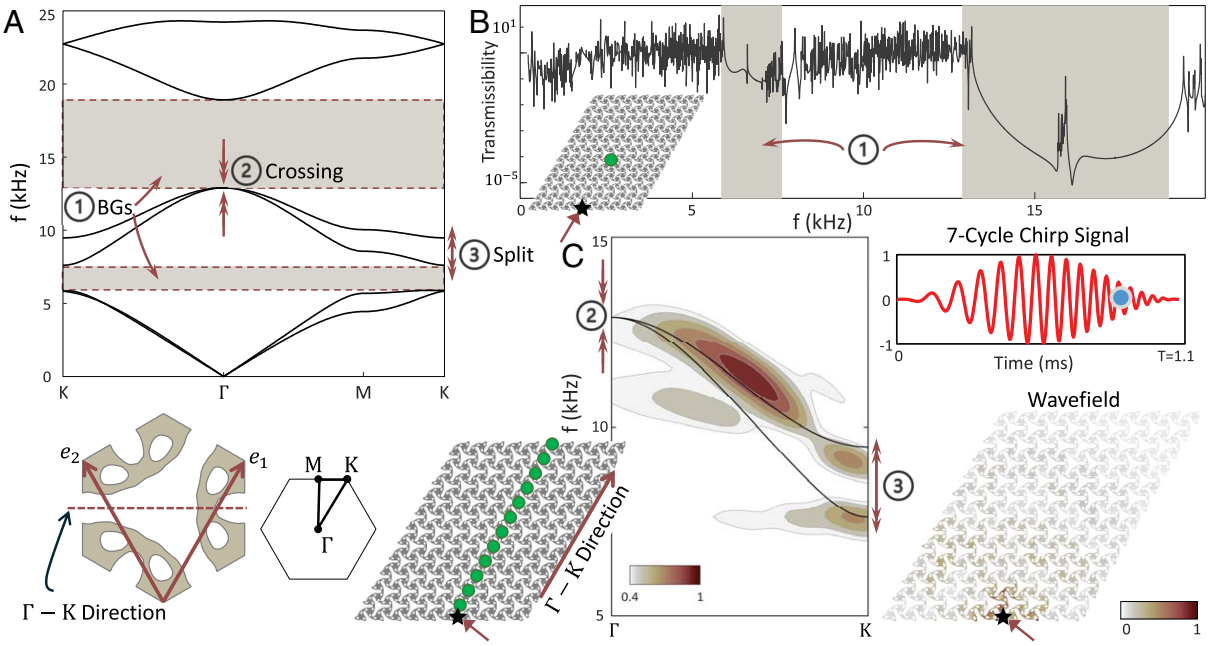

Fig. 3. Optimized design exhibiting target topological bands. (*A*) Unit cell derived from the topology optimization algorithm, shown with its calculated band diagram. The mid-frequency bands demonstrate the desired morphological attributes, with the Brillouin zone indicated in the *Inset*. (*B*) Transmissibility versus frequency plot, illustrating the formation of two bandgaps (BGs) enclosing finite-frequency passing bands. (*C*) Band reconstruction from transient simulations using a chirp signal (plotted in red), capturing key morphological features of bands 3 to 4, specifically the crossing at Γ and splitting at K, accompanied by a snapshot of the associated wavefield.

and K (see *SI Appendix* for details on the irreps and mode shapes at the HSPs calculated for this configuration, and the existence of localized modes within the BGs). To corroborate these band characteristics, we conduct full-scale FE simulations on a finite domain obtained via 2D tessellation of the optimized unit cell. Specifically, to capture the first requirement (isolated finite-frequency bands), we perform a frequency-domain simulation under sustained harmonic excitation. The domain is excited at the black star (input) and the response is measured at the green dot (output) of the *Inset* of Fig. 3*B*. By sweeping the frequency and calculating, for each ω, the output/input ratio, we generate the transmissibility curve shown in Fig. 3*B*. This curve confirms two attenuation regions (shaded), matching the BG frequencies predicted by Bloch analysis and sandwiching a pass-band region.

To document the second and third features (band crossing pattern), we need to reconstruct the actual morphology of the bands. To this end, we resort to transient simulations to induce waves with a broad wavevector content and we sample them along specific directions corresponding to given intervals of the BZ contour. We excite the domain at the black star (*Inset* of Fig. 3*C*) with a 7-cycle linear chirp signal polarized perpendicular to the Γ−K direction, as shown in red in Fig. 3*C*. The instantaneous frequency is defined as $f(t) = ct + f_0$, where $f_0 = 6.5$ kHz is the starting frequency, $f_1 = 26$ kHz is the final frequency, $c = \frac{f_1 - f_0}{T}$ is the chirp rate, and $T = 1.1$ ms is the total sweep time. A snapshot of the wavefield at the time corresponding to the blue point in the signal plot is also shown in Fig. 3*C*, with color map corresponding to the normalized displacement magnitude. We collect displacement time histories at discrete, equally spaced points along Γ−K (green dots in Fig. 3 *C*, *Inset*), and perform 2D discrete Fourier transform (DFT) to transform the spatiotemporal dataset into a frequency-wavenumber dataset. The resulting spectral amplitude contours, overlaid on the band structure in Fig. 3*C*, confirm the targeted morphological characteristics, with a single prominent spectral feature at Γ and, in contrast, a split signature at K with two spectral features conforming to the limits of bands 3 and 4, respectively.

To confirm the robustness of the established topological signatures of the optimized configuration in transitioning from ideal simulations to physical implementations, we now complement our numerical predictions with experimental validation using laser vibrometry [Polytec PSV 400 3D Scanning Laser Doppler Vibrometer (SLDV)] on a physical prototype. The experimental setup is illustrated in Fig. 4*A*, with a zoomed-in view of the waterjet-cut prototype geometry shown in the *Inset* of Fig. 4*B* (all details provided in *Materials and Methods*). The experiments confirm the emergence of the key dynamical features associated with topological bands at finite frequencies for this symmetry class. First, we apply a broadband pseudorandom excitation at the point marked by the black star in Fig. 4*C*, and we measure the in-plane velocity at selected sampling points within the white box. The experimentally reconstructed transmissibility curve reveals the opening of two BGs, confining a pass-band region, with excellent qualitative and satisfactory quantitative match of its numerical counterpart. Next, in Fig. 4*D*, we experimentally reconstruct the bands 3 to 4 morphology by exciting the frequency range of the bands using three concatenated 7-cycle narrow-band tone burst excitations with carrier frequencies of 8.5 kHz, 10 kHz, and 13 kHz, and sampling the response along the relevant lattice direction. The spectral amplitude maps conform to the bands predicted by Bloch analysis, confirming the crossing at Γ and the split at K. The FFT spectra of the tone bursts, shown in the *Right* panel of Fig. 4*D*, are color-coded to highlight the corresponding frequency intervals with the top 40% activation.

Design Space Exploration and Construction of Configuration Libraries. Next, we explore the design space to identify alternative configurations that belong to the same symmetry class and preserve the band morphology characteristics necessary for the existence of topologically nontrivial states. The broader objective

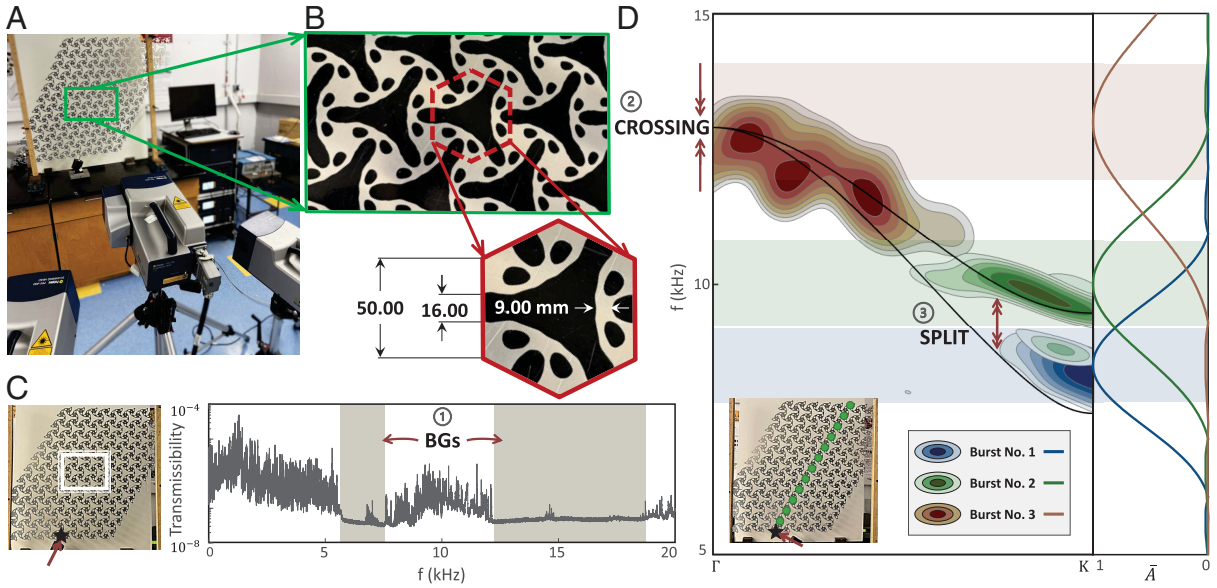

Fig. 4. Experiments confirming the emergence of topological signatures: prototype of a fabricated lattice following result from topology optimization algorithm. (*A* and *B*) Experimental setup for 3D Scanning Laser Doppler Vibrometer testing and a close-up view of the specimen, with the geometric details of its corresponding unit cell shown in the *Inset*. (*C*) Experimental transmissibility curve revealing finite-frequency pass-band between bandgaps (BGs). (*D*) Experimentally reconstructed band morphology featuring crossing at Γ and split at K, revealing signatures of nontrivial topology according to topological quantum chemistry irreducible representations. The spectra of the excitation signals are shown on the *Right*, with color-coded regions indicating the frequency intervals of highest activation for each tone.

of this design exploration is to demonstrate the capability of this framework to discover, as a result of a simple parameter calibration, an entire library of configurations that share common topological attributes and simultaneously achieve a plethora of secondary phononic characteristics. The chart in Fig. 5 illustrates a collection of optimized configurations obtained

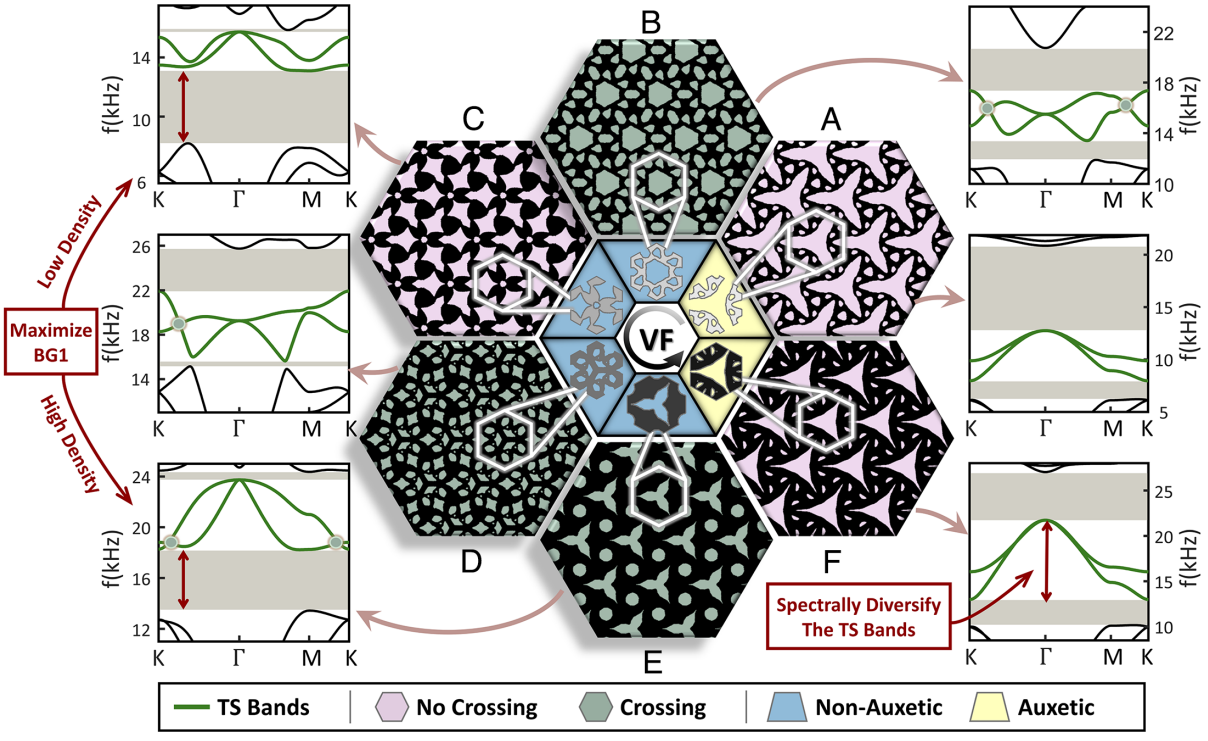

Fig. 5. (*A-F*) A diverse library of discovered metamaterials that share common topological attributes, illustrated using results for the benchmark symmetry class. The optimized unit cells and their tessellated configurations are organized by volume fraction (VF). The corresponding band diagram for each case is presented within the frequency range of the topological states (TSs) (green lines). All cases are color-coded to indicate the presence or absence of additional crossings at wave vectors along the high-symmetry lines. Cases A and F are auxetic, while Cases B to E have a positive Poisson's ratio and are shaded accordingly. Although the designs retain the same topological character due to enforced band morphology constraints, they exhibit distinct geometric variations.

through parameter and formulation alteration in the TO problem that result in lattices with different volume fractions (VFs) (either by design, by imposing desired bounds on VF as constraints, or as a spontaneous byproduct of the algorithm targeting some functionalities objectives). Six optimized unit cells are shown in six trapezoidal boxes organized counterclockwise according to their VF. For each configuration, the resulting tessellation is shown in the corresponding hexagonal sector of the chart to highlight the variety of patterns and connectivity landscapes that can be achieved. For each case, we report a portion of the corresponding band diagram corresponding to the frequency range that encompasses the TSs (highlighted) to emphasize that in all cases the common morphological band features enforced by the algorithm are indeed met. The explored variations include adjusting design parameters such as BG width and VF, swapping objectives and constraints, or imposing additional constraints. See *SI Appendix* on the specific TO formulations used in each case.

Interestingly, even slight modifications to the TO formulation lead to significant changes in both the real-space geometry and the reciprocal-space band structure due to the highly nonconvex nature of the mathematical optimization problem, with influences on the phononic or mechanical properties. An intriguing occurrence is the appearance of additional band crossings along the high-symmetry lines Γ−K and/or M−K. This feature is observed in Cases B, D, and E. Cases featuring crossing are highlighted in Fig. 5 by green backgrounds in the tessellations against pink backgrounds for the regular cases. Notably, these crossings not occurring at the HSPs do not alter the topological character of the bands. Therefore, these cases are correctly obtained by the algorithm. It is also interesting to see how different configurations can be classified according to their bulk, shear moduli, and Poisson's ratio. These quantities can be inferred from a manipulation of the wave speeds of the acoustic modes in the long-wavelength limit, as discussed in ref. 71. Remarkably, Cases A and F, which have the most kagome-like geometries, exhibit auxetic behavior (shaded light yellow in Fig. 5), whereas the other cases have a positive Poisson's ratio (shaded blue in Fig. 5). See *SI Appendix* for more details. Additional differences between these outcomes can be pointed out that can be traced to differences in the TO algorithm. Cases C and E share similar TO formulations, both aiming to maximize BG1 while maintaining a similar lower bound constraint on VF. However, in Case C, the algorithm allows lower values for BG2, ultimately yielding two design options: one with a lower effective mass density (C) and another with a higher effective mass density (E). Case D is designed to simultaneously maximize the gaps at the HSPs between bands 2 to 3 and 4 to 5, while enforcing all other requirements as constraints. Last, Case F is designed to enhance experimental feasibility by optimizing the TSs for maximum bandwidth. In other words, we increase the spectral separation between the peak and valley frequencies of the TSs to facilitate experimental validation and simplify testing.

The designs in Fig. 5 have different lattice layouts but share the same topological band features, highlighting the highly nonconvex nature of the design space. Here, we embrace this nonconvexity and find various nonunique solutions via alterations of optimization formulations, initial guesses, and optimization parameters. Although a formal proof of convergence and stability is beyond the scope of this study, the proposed framework appears effective in generating diverse topological metamaterials, as it successfully produces different designs in a nonconvex design space for both simple (in Fig. 2) and complex design goals (in Fig. 5). Nevertheless, some adjustments for the design criteria, especially for desired constraint tolerances, might be required to successfully obtain an optimized design. An informed choice of initial guess, particularly for more demanding design criteria, can also expedite the discovery of topological metamaterials. For example, we obtained the optimized design in Fig. 2 from a uniform initial guess (i.e., $\boldsymbol{z} = 0.5$), and subsequently used it as the initial guess for case F of Fig. 5 that has a larger HSP gap requirements (*SI Appendix*, Table S1).

Concluding Remarks

TO has emerged as a powerful tool for designing metamaterials with tailored mechanical and wave manipulation properties. While significant progress has been made in optimizing conventional performance metrics-such as stiffness, toughness, and BG width-the systematic integration of topological constraints into TO frameworks remains largely unexplored. This gap stems from the inherent challenge of mathematically formulating topological requirements in a rigorous and computationally tractable manner. In this work, we have addressed these challenges by introducing a methodology that seamlessly integrates band topology criteria into TO algorithms. Leveraging the framework of TQC, we have identified key band morphological attributes that serve as reliable indicators of topological character. Beyond its theoretical contributions, this study enables the automated generation of metamaterials with on-demand topological properties, bridging the gap between theoretical predictions and experimental realization. As a proof of concept, we showcase a diverse set of lattice configurations-each engineered to satisfy a complementary wave manipulation property while constrained to the same primary topology, thereby establishing a structured approach to metamaterial discovery.

Importantly, the framework introduced in this work, while conceived in the context of lattices with the $p31m$ wallpaper group, is extendable in principle to a broader class of lattices, encompassing all 2D symmorphic elastic lattices. We note, however, that generalizing the approach beyond $p31m$, while technically feasible, is a nuanced operation that would generally require some additional steps. In particular, inverse design methods-such as TO-for lattices with other symmetry groups would necessitate the incorporation of constraints that enforce the symmetry properties of the eigenfunctions-specifically, how they transform under point group operations such as rotations or reflections (i.e., whether they are even or odd under a given symmetry operation). While the current implementation operates solely on eigenvalues, our algorithm solves the full eigenvalue problem, yielding both eigenvalues and eigenvectors at each iteration, so it is equipped with the ability to generate the computational outputs required by this extended analysis. Note that, even working with more complex wallpaper groups, the band morphology attributes would remain a useful heuristic that offers meaningful guidance and the analysis would still be hinged on morphological band assessment along the lines discussed in this manuscript. However, enforcing eigenfunction symmetries at HSPs within the optimization algorithm would be an essential additional step. Importantly, these constraints would only need to be applied at a small number of wavevectors (at HSPs), so the additional computational cost would remain modest and the entire procedure tractable.

Materials and Methods

Simulation and Optimization Setup. We generate a quadrilateral isoparametric mesh with approximately 14,000 elements within a hexagonal unit cell domain, where each side is set to unity (Fig. 2*A*). The mesh is refined appropriately

while preserving the targeted symmetry group, C_{3v}. To construct the symmetric mesh, we first discretize the highlighted region in Fig. 2*A* using GMSH. We then apply the mirror symmetry operation m_{11}, reflecting the mesh across the plane perpendicular to $\mathbf{e}_1 + \mathbf{e}_2$. Subsequently, we apply two successive rotations, C_3^1 and C_3^2, to generate a symmetric mesh across the entire domain. Details of the TO, including design parameterization, interpolation rules between solid and void properties (72, 73), and optimization formulations alternative to Eq. **4** are provided in *SI Appendix*.

Material Properties and Optimized Unit Cell Specification. The optimization process yields a pixelated black-and-white hexagon unit cell (Fig. 2*C*), where black and white regions correspond to solid and void, respectively. Due to the jagged nature of the boundaries, we import the geometry into SolidWorks and smooth the edges using splines. The smoothed domain is then scaled so that each side of the hexagon measures 50 mm. For band structure computations, the smoothed domain is exported as a .STEP file and imported into GMSH for meshing. We discretize the unit cell into approximately 2,880 elements using 4-node isoparametric quadrilateral elements under a 2D plane stress assumption. Each node has two in-plane translational degrees of freedom, and a unit thickness is assumed. The material is modeled as linearly elastic and isotropic, and we use standard numerical integration (2×2 Gauss quadrature) to assemble the global stiffness and mass matrices. A canonical Bloch periodic boundary condition is applied along the unit cell edges. The resulting eigenvalue problem is solved to obtain the phonon band diagrams. For full-scale simulation analysis, we tessellate the unit cell to construct a finite parallelogram domain consisting of 120 unit cells. For experimental testing, the finite domain geometry is exported as an .STL file for manufacturing. Fig. 4 *A* and *B* show the fabricated specimen, produced via water-jet cutting from a 2-mm-thick aluminum sheet, which is vertically constrained via boundary supports. The material properties of aluminum are Young's modulus = 71 GPa, Poisson's ratio = 0.33, and mass density = 2,700 kg/m^3.

The 3D Laser Doppler Vibrometer Experiments. The Polytec PSV 400 3D SLDV, equipped with three scanning laser heads, is used to acquire in-plane velocity measurements at predefined scan points. Excitation is applied via an electromechanical shaker (Brüel & Kjær Type 4810), which is internally triggered by the vibrometry setup through an amplifier (Brüel & Kjær Type 2718). The shaker excites the lattice through a stinger at the desired location. Retroreflective tape is applied at the scan points to enhance reflectivity and reduce noise in the data. The acquired velocity data are decomposed into $\hat{x}$, $\hat{y}$, and $\hat{z}$ components using Euler angles, which are internally computed by the PSV software as part of the 3D alignment process. These data are further processed in MATLAB to construct the transmissibility curve and reconstruct wavefields and DFT plot.

To experimentally construct the transmissibility curve, we apply the excitation signal in the 0 to 20 kHz range in three subranges: 0 to 5 kHz, 5 to 10 kHz, and 10 to 20 kHz. To ensure sufficient energy is supplied at higher frequencies, we prescribe progressively higher amplitudes for each successive range, allowing for a more uniform energy injection across the entire spectrum. To reconstruct the TSs along the $\Gamma-$K direction, we note that this direction aligns with the lattice vector $\mathbf{e}_1$ (*Inset* of Fig. 3*A*). Therefore, we measure the time histories of the $\hat{x}$ and $\hat{y}$ in-plane velocity components at 12 equally spaced scan points along the $\Gamma-$K direction and separated by the magnitude of the primitive lattice vector $\mathbf{e}_1$ (green dots in the *Inset* of Fig. 4*D*). To mitigate the influence of low-frequency ambient vibrations, we apply a high-pass filter embedded in the vibrometry software. The resulting spatiotemporal data are then subjected to a 2D-DFT to obtain the spectral amplitude contours shown in Fig. 4*D*.

Data, Materials, and Software Availability. Some study data are available: SLDV data and meshes from FEM simulations due to the large file size will be made available upon request. All other data are included in the manuscript and/or *SI Appendix*.

ACKNOWLEDGMENTS. P.A. acknowledges the support of the University of Minnesota College of Science and Engineering Graduate Fellowship. P.A. and S.G. acknowledge support from the NSF (grant CMMI-2027000 and CMMI-2344257). R.D.K., W.L., and X.S.Z. acknowledge support from the Air Force Office of Scientific Research (award FA9550-23-1-0297) and NSF (grant CMMI-2344258) and K.S. acknowledges the support from the Office of Naval Research (grant MURI N00014-20-1-2479).

Author affiliations: [a]Department of Civil, Environmental, and Geo- Engineering, University of Minnesota, Minneapolis, MN 55455; [b]Department of Civil and Environmental Engineering, University of Illinois at Urbana-Champaign, Urbana, IL 61801; and [c]Department of Physics, University of Michigan, Ann Arbor, MI 48109

Author contributions: P.A., R.D.K., W.L., K.S., X.S.Z., and S.G. designed research; P.A. and R.D.K. performed research; P.A., R.D.K., and W.L. analyzed data; P.A. performed experiments; W.L., K.S., X.S.Z., and S.G. edited the paper; and P.A., R.D.K., and S.G. wrote the paper.

1. Y. Li, E. Baker, T. Reissman, C. Sun, W. K. Liu, Design of mechanical metamaterials for simultaneous vibration isolation and energy harvesting. *Appl. Phys. Lett.* **111**, 251903 (2017).
2. X. Fang, K. C. Chuang, X. Jin, Z. Huang, Band-gap properties of elastic metamaterials with inerter-based dynamic vibration absorbers. *J. Appl. Mech.* **85**, 071010 (2018).
3. C. Sugino, M. Ruzzene, A. Erturk, Merging mechanical and electromechanical bandgaps in locally resonant metamaterials and metastructures. *J. Mech. Phys. Solids* **116**, 323–333 (2018).
4. B. Florijn, C. Coulais, M. van Hecke, Programmable mechanical metamaterials. *Phys. Rev. Lett.* **113**, 175503 (2014).
5. R. Zhu, X. N. Liu, G. K. Hu, C. T. Sun, G. L. Huang, Negative refraction of elastic waves at the deep-subwavelength scale in a single-phase metamaterial. *Nat. Commun.* **5**, 5510 (2014).
6. K. Bertoldi, V. Vitelli, J. Christensen, M. van Hecke, Flexible mechanical metamaterials. *Nat. Rev. Mater.* **2**, 17066 (2017).
7. X. Yu, J. Zhou, H. Liang, Z. Jiang, L. Wu, Mechanical metamaterials associated with stiffness, rigidity and compressibility: A brief review. *Prog. Mater. Sci.* **94**, 114–173 (2018).
8. J. U. Surjadi *et al*., Mechanical metamaterials and their engineering applications. *Adv. Eng. Mater.* **21**, 1800864 (2019).
9. N. N. Stenseng, M. M. Samak, O. R. Bilal, Bi-stable metamaterials with intrinsic memory for selective wave filtering based on frequency and amplitude. *Adv. Sci.* **12**, 2405146 (2024).
10. C. L. Kane, T. C. Lubensky, Topological boundary modes in isostatic lattices. *Nat. Phys.* **10**, 39–45 (2014).
11. D. Z. Rocklin, S. Zhou, K. Sun, X. Mao, Transformable topological mechanical metamaterials. *Nat. Commun.* **8**, 14201 (2017).
12. R. K. Pal, M. Ruzzene, Edge waves in plates with resonators: An elastic analogue of the quantum valley hall effect. *New J. Phys.* **19**, 025001 (2017).
13. J. Vila, R. K. Pal, M. Ruzzene, Observation of topological valley modes in an elastic hexagonal lattice. *Phys. Rev. B* **96**, 134307 (2017).
14. M. Yan *et al*., On-chip valley topological materials for elastic wave manipulation. *Nat. Mater.* **17**, 993–998 (2018).
15. S. Y. Yu *et al*., Elastic pseudospin transport for integratable topological phononic circuits. *Nat. Commun.* **9**, 3072 (2018).
16. S. H. Mousavi, A. B. Khanikaev, Z. Wang, Topologically protected elastic waves in phononic metamaterials. *Nat. Commun.* **6**, 8682 (2015).
17. M. Xiao *et al*., Geometric phase and band inversion in periodic acoustic systems. *Nat. Phys.* **11**, 240–244 (2015).
18. C. He *et al*., Acoustic topological insulator and robust one-way sound transport. *Nat. Phys.* **12**, 1124–1129 (2016).
19. L. M. Nash *et al*., Topological mechanics of gyroscopic metamaterials. *Proc. Natl. Acad. Sci. U.S.A.* **112**, 14495–14500 (2015).
20. B. Bradlyn *et al*., Topological quantum chemistry. *Nature* **547**, 298–305 (2017).
21. M. G. Vergniory *et al*., Graph theory data for topological quantum chemistry. *Phys. Rev. E* **96**, 023310 (2017).
22. J. Cano *et al*., Building blocks of topological quantum chemistry: Elementary band representations. *Phys. Rev. B* **97**, 035139 (2018).
23. J. Kruthoff, J. de Boer, J. van Wezel, C. L. Kane, R. J. Slager, Topological classification of crystalline insulators through band structure combinatorics. *Phys. Rev. X* **7**, 041069 (2017).
24. H. C. Po, A. Vishwanath, H. Watanabe, Symmetry-based indicators of band topology in the 230 space groups. *Nat. Commun.* **8**, 1–9 (2017).
25. H. C. Po, Symmetry indicators of band topology. *J. Phys. Condens. Matter* **32**, 263001 (2020).
26. E. Khalaf, H. C. Po, A. Vishwanath, H. Watanabe, Symmetry indicators and anomalous surface states of topological crystalline insulators. *Phys. Rev. X* **8**, 031070 (2018).
27. B. Bradlyn, Z. Wang, J. Cano, B. A. Bernevig, Disconnected elementary band representations, fragile topology, and wilson loops as topological indices: An example on the triangular lattice. *Phys. Rev. B* **99**, 045140 (2019).
28. Z. D. Song, L. Elcoro, B. A. Bernevig, Twisted bulk-boundary correspondence of fragile topology. *Science* **367**, 794–797 (2020).
29. M. I. Aroyo *et al*., Crystallography online: Bilbao crystallographic server. *Bulg. Chem. Commun* **43**, 183–197 (2011).
30. M. I. Aroyo *et al*., Bilbao crystallographic server: I. Databases and crystallographic computing programs. *Z. Kristallogr. Cryst. Mater.* **221**, 15–27 (2006).
31. M. I. Aroyo, A. Kirov, C. Capillas, J. Perez-Mato, H. Wondratschek, Bilbao crystallographic server. II. Representations of crystallographic point groups and space groups. *Acta Crystallogr. A Found. Crystallogr.* **62**, 115–128 (2006).
32. L. Elcoro *et al*., Double crystallographic groups and their representations on the Bilbao Crystallographic Server. *J. Appl. Crystallogr.* **50**, 1457–1477 (2017).

33. S. Bird *et al.*, Design and characterization of all two-dimensional fragile topological bands. arXiv [Preprint] (2024). https://arxiv.org/abs/2410.10484 (Accessed 15 October 2024).
34. M. B. de Paz, M. G. Vergniory, D. Bercioux, A. García-Etxarri, B. Bradlyn, Engineering fragile topology in photonic crystals: Topological quantum chemistry of light. *Phys. Rev. Res.* **1**, 032005 (2019).
35. V. Peri *et al.*, Experimental characterization of fragile topology in an acoustic metamaterial. *Science* **367**, 797–800 (2020).
36. S. Sarkar, "Multipoles, symmetry representations and thermal fluctuations in elastic systems," PhD thesis, Princeton University (2021).
37. P. Azizi, S. Sarkar, K. Sun, S. Gonella, Dynamics of self-dual Kagome metamaterials and the emergence of fragile topology. *Phys. Rev. Lett.* **130**, 156101 (2023).
38. Z. D. Zhang, M. H. Lu, Y. F. Chen, Twist-angle-induced boundary-obstructed topological insulator on elastic Kagome metamaterials. *Phys. Rev. Appl.* **20**, 054002 (2023).
39. P. Azizi, S. Sarkar, K. Sun, S. Gonella, Omnidirectional domain wall modes protected by fragile topological states. *Phys. Rev. B* **110**, L060102 (2024).
40. M. P. Bendsøe, N. Kikuchi, Generating optimal topologies in structural design using a homogenization method. *Comput. Methods Appl. Mech. Eng.* **71**, 197–224 (1988).
41. M. P. Bendsøe, O. Sigmund, *Topology Optimization* (Springer, Berlin Heidelberg, 2004).
42. C. Wang, Z. Zhao, M. Zhou, O. Sigmund, X. S. Zhang, A comprehensive review of educational articles on structural and multidisciplinary optimization. *Struct. Multidiscip. Optim.* **64**, 2827–2880 (2021).
43. O. Sigmund, J. S. Jensen, Systematic design of phononic band-gap materials and structures by topology optimization. *Philos. Trans. R. Soc. A* **361**, 1001–1119 (2003).
44. A. Dalklint, M. Wallin, K. Bertoldi, D. Tortorelli, Tunable phononic bandgap materials designed via topology optimization. *J. Mech. Phys. Solids* **163**, 104849 (2022).
45. J. Liu, S. Li, Efficient phononic band gap optimization in two-dimensional lattice structures using extended multiscale finite element method. *Struct. Multidiscip. Optim.* **67**, 166 (2024).
46. H. W. Dong *et al.*, Inverse design of phononic meta-structured materials. *Mater. Today* **80**, 824–855 (2024).
47. K. Wang, Y. Liu, B. Wang, Ultrawide band gap design of phononic crystals based on topological optimization. *Phys. B Condens. Matter* **571**, 263–272 (2019).
48. Y. Luo, Y. Li, Tunable bandgap design of soft phononic crystals using topology optimization. *Adv. Theory Simul.* **5**, 2100620 (2022).
49. Q. Wu, J. He, W. Chen, Q. Li, S. Liu, Topology optimization of phononic crystal with prescribed band gaps. *Comput. Methods Appl. Mech. Eng.* **412**, 116071 (2023).
50. S. L. Vatanabe, G. H. Paulino, E. C. N. Silva, Maximizing phononic band gaps in piezocomposite materials by means of topology optimization. *J. Acoust. Soc. Am.* **136**, 494–501 (2014).
51. Z. Jia *et al.*, Maximizing acoustic band gap in phononic crystals via topology optimization. *Int. J. Mech. Sci.* **270**, 109107 (2024).
52. R. E. Christiansen, O. Sigmund, Designing meta material slabs exhibiting negative refraction using topology optimization. *Struct. Multidiscip. Optim.* **54**, 469–482 (2016).
53. R. E. Christiansen, B. S. Lazarov, J. S. Jensen, O. Sigmund, Creating geometrically robust designs for highly sensitive problems using topology optimization: Acoustic cavity design. *Struct. Multidiscip. Optim.* **52**, 737–754 (2015).
54. F. Wang, R. E. Christiansen, Y. Yu, J. Mørk, O. Sigmund, Maximizing the quality factor to mode volume ratio for ultra-small photonic crystal cavities. *Appl. Phys. Lett.* **113**, 241101 (2018).
55. C. Van hoorickx, O. Sigmund, M. Schevenels, B. Lazarov, G. Lombaert, Topology optimization of two-dimensional elastic wave barriers. *J. Sound Vib.* **376**, 95–111 (2016).
56. K. Matsushima, H. Isakari, T. Takahashi, T. Matsumoto, A topology optimisation of composite elastic metamaterial slabs based on the manipulation of far-field behaviours. *Struct. Multidiscip. Optim.* **63**, 231–243 (2020).
57. R. E. Christiansen, F. Wang, O. Sigmund, Topological insulators by topology optimization. *Phys. Rev. Lett.* **122**, 234502 (2019).
58. S. Nanthakumar *et al.*, Inverse design of quantum spin hall-based phononic topological insulators. *J. Mech. Phys. Solids* **125**, 550–571 (2019).
59. Y. Chen, F. Meng, X. Huang, Creating acoustic topological insulators through topology optimization. *Mech. Syst. Signal Process.* **146**, 107054 (2021).
60. Y. Lu, H. S. Park, Double Dirac cones and topologically nontrivial phonons for continuous square symmetric $C_{4(v)}$ and $C_{2(v)}$ unit cells. *Phys. Rev. B* **103**, 064308 (2021).
61. R. E. Christiansen, F. Wang, O. Sigmund, S. Stobbe, Designing photonic topological insulators with quantum-spin-hall edge states using topology optimization. *Nanophotonics* **8**, 1363–1369 (2019).
62. X. Zhuang *et al.*, Inverse design of reconfigurable piezoelectric topological phononic plates. *Mater. Des.* **219**, 110760 (2022).
63. J. Zhang, F. Wang, O. Sigmund, L. Gao, R. E. Christiansen, Ultra-broadband edge-state pair for zigzag-interfaced valley hall insulators. *Sci. China Phys. Mech. Astron.* **65**, 257011 (2022).
64. J. Luo *et al.*, Efficient design of helical higher-order topological insulators in 3D elastic medium. *J. Mech. Phys. Solids* **176**, 105325 (2023).
65. G. Kreisselmeier, R. Steinhauser, Systematic control design by optimizing a vector performance index. *IFAC Proc. Vol.* **12**, 113–117 (1979).
66. T. E. Bruns, D. A. Tortorelli, Topology optimization of non-linear elastic structures and compliant mechanisms. *Comput. Methods Appl. Mech. Eng.* **190**, 3443–3459 (2001).
67. B. Bourdin, Filters in topology optimization. *Int. J. Numer. Meth. Eng.* **50**, 2143–2158 (2001).
68. O. Sigmund, Morphology-based black and white filters for topology optimization. *Struct. Multidiscip. Optim.* **33**, 401–424 (2007).
69. C. Talischi, G. H. Paulino, A. Pereira, I. F. M. Menezes, Polytop: A matlab implementation of a general topology optimization framework using unstructured polygonal finite element meshes. *Struct. Multidiscip. Optim.* **45**, 329–357 (2012).
70. F. Wang, B. S. Lazarov, O. Sigmund, On projection methods, convergence and robust formulations in topology optimization. *Struct. Multidiscip. Optim.* **43**, 767–784 (2010).
71. A. S. Phani, J. Woodhouse, N. A. Fleck, Wave propagation in two-dimensional periodic lattices. *J. Acoust. Soc. Am.* **119**, 1995–2005 (2006).
72. M. Zhou, G. Rozvany, The COC algorithm, part II: Topological, geometrical and generalized shape optimization. *Comput. Methods Appl. Mech. Eng.* **89**, 309–336 (1991).
73. M. P. Bendsøe, O. Sigmund, Material interpolation schemes in topology optimization. *Arch. Appl. Mech. Ingenieur Arch.* **69**, 635–654 (1999).